Microstructure, Hardness, and Residual Stress of the Dissimilar Metal Weldments of SA508-309L/308L-304L

WEICHENG ZHONG, JUN-LI LIN, YAN CHEN, ZHEN LI, KE AN, BENJAMIN J. SUTTON, and BRENT J. HEUSER

A dissimilar metal weldment consisting of SA508-309L-308L-304L is widely used in light-water nuclear reactors. These weldments demonstrate dissimilar susceptibility to stress corrosion cracking that are related to the microstructure, properties, and residual stress. In this work, microstructures, hardness, and the residual stress distribution of the dissimilar metal weldments were investigated, with the correlation of increased hardness in the heat-affected zone (HAZ) to the microstructure. 304L HAZ demonstrated similar grain morphology as the base material, and the increase in hardness was primarily attributed to the increased dislocation density. SA508 HAZ demonstrated a change of grain morphology resulting from the different peak temperatures and cooling rates. The increased hardness in the SA508 HAZ was attributed to the refined grain morphology, higher dislocation density, and higher number density of precipitates. A ~ 20–30-μm-wide martensitic zone formed at the fusion boundary of SA508-309L, where Cr-rich carbide precipitates were observed, with the average size and the number density of 44.1 ± 16.9 nm and 1.5×10^{21} m^{-3}, respectively. Residual stress results demonstrated the largest tensile stress at 309L butter, indicating its high cracking susceptibility.

https://doi.org/10.1007/s11661-021-06203-x

I. INTRODUCTION

IN the light-water reactors (LWRs) in nuclear industry, low-alloy ferritic steels SA508 are widely used for pressure vessels and steam generators for decades due to their low cost and adequate mechanical properties,[1] while Fe-Cr-Ni austenitic stainless steels (SS), such as SS 304L, are used extensively as piping and core internal due to their high corrosion resistance.[2] The joining of two different components is necessary, which is typically performed using welding techniques. Dissimilar metal weldments (DMWs) between ferritic and austenitic materials require filler/butter materials that are compatible to both base materials to account for the composition, crystallographic structure, and thermal properties mismatch of the two base materials. SS 308L filler with SS 309L butter is one of the filler/butter combinations extensively used in nuclear industry. While both SA508 and SS 304L base materials performed favorably in LWRs environment, significantly reduced lifetimes have been reported on the DMWs that originated from stress corrosion cracking.[3,4] Cracking behaviors are complex phenomena that are directly affected by the microstructure, mechanical properties, and the residual stress of the welded components. Therefore, understanding the evolution of microstructure, mechanical properties, and residual stress distribution from the welding process is important.

Materials are subjected to cyclical thermal cycles from the welding process, which alters the mechanical properties of regions near weldments and leads to local

WEICHENG ZHONG is with Oak Ridge National Laboratory, Oak Ridge, TN, 37830 and also with the University of Illinois, Urbana-Champaign, Urbana, IL, 61801. Contact e-mail: zhongw@ornl.gov. JUN-LI LIN, ZHEN LI and BRENT J. HEUSER are with the University of Illinois, Urbana-Champaign. Contact e-mail: bheuser@illinois.edu YAN CHEN and KE AN are with the Oak Ridge National Laboratory. BENJAMIN J. SUTTON is with the Electric Power Research Institute, Charlotte, NC, 28262.

Manuscript submitted 23 September 2020; accepted 13 February 2021

Article published online March 15, 2021

microstructural heterogeneity that is known as heat-affected zone (HAZ). Two HAZs form in DWMs; one at low-alloy ferritic steels, and the other at austenitic SS. Increased hardness in HAZ of low-alloy ferritic steels was consistently reported.[5–8] Complex microstructures were observed at different regions within HAZ that were originated from the different peak temperatures/cooling rates and from the composition gradient due to the composition mismatch. Such complex microstructures affected the mechanical response of the components.[5,8–10] For example, carbon diffusion from low-alloy steels lead to the formation of a carbon-depleted zone where lower hardness was reported.[7] The composition gradient in addition to the rapid cooling rate lead to the formation of a narrow martensitic zone at the fusion boundary,[6,7,11] where loss of ductility and increase of hardness were reported.[12]

Unlike the HAZ of low-alloy ferritic steels, the hardness in the HAZ of austenitic SS showed different results, with both an increase[7,13,14] and a decrease [2,15,16] reported in the HAZ of austenitic SS, likely due to the different welding techniques and/or processing parameters. High-energy welding techniques, such as laser welding, lead to completely different grain morphology in the HAZ,[13] whereas no significant change of the grain morphology was observed for lower energy welding, such as gas tungsten arc welding (GTAW). While the microstructure was correlated to hardness in laser weld HAZ of the austenitic SS 304,[13] such a correlation was not investigated for the HAZ of low-alloy ferritic steels and for the GTAW HAZ of austenitic SS, which maintains similar grain morphology as the base materials.

Residual stress in the weld joints is known to affect the cracking behavior, and thus the lifetime of the weld components.[17–19] Tensile residual stress is recognized as one of the major failure mechanisms in weldments.[20] Therefore, it is critical to understand the residual stress accumulation from the welding process. One recent study on the stress corrosion cracking of SA508-309L/308L-316L weldments showed different susceptibilities at different regions, with highest susceptibility on the 309L butter.[3] While microstructures were investigated to explain the SCC behavior, the residual stress contribution to SCC was neglected. Prior residual stress work has focused on DMWs with Ni-based austenitic filler,[19,21] while the effect of residual stress of DMWs with Fe-based austenitic SS filler is lacking in the published literature.

Comprehensive knowledge of the microstructure, mechanical properties, and residual stress distributions is important to understand weldment performance. In this work, we studied the dissimilar metal weld of SA508 and austenitic SS 304L using SS 309L butter and SS 308L filler. Residual stress distributions across the weldment were characterized using the neutron diffraction technique. Microstructure and hardness were investigated at different regions across the weldment, with particular focus on the HAZ of SA508 and SS 304L. The change of hardness in the HAZ was qualitatively correlated with the microstructure evolution from the welding process.

II. MATERIALS AND METHODS

A. *The Compositions and Heat Treatment of the Weldment*

Figure 1 is a schematic illustration of the DMW studied in this work that was fabricated using the GTAW technique. SA508 was joined with SS 304L using the SS 308L filler and SS 309L butter adjacent to the SA508. The compositions of each material are provided in Table I, along with the calculated Cr and Ni equivalent compositions based on the Welding Research Council 1992 (WRC-1992) constitution diagram.[22] The nitrogen concentrations in SS 308L and SS 309L were not measured, and a reasonable estimate of ~ 0.05 wt pct nitrogen concentration is assumed for the purpose of the equivalent Cr (Cr_{eq}) and Ni (Ni_{eq}) compositions calculation. A total of 54 bead lines of SS 309L butter were deposited in five layers on SA508 with the interpass temperature of 177 °C. The current average, voltage average, average travel speed were 215 A, 9.9 V, and 8.1 cm/min, respectively. A post-weld heat treatment (PWHT) was performed on the SA508 plate with 309L butter at 635 ± 10 °C for 1.5 hours. The heat-up and cool-down temperature ramp rates were below 70 °C/h when the temperature was above 220 °C. The butter was then cut to an approximate thickness of 15.6 mm. The 308L filler weld consisted of a total of 57 bead lines in 18 layers and the interpass temperature was 177 °C. The fit-up root opening was 3.2 mm and the fit-up width at the joint top was 32 mm. The current, voltage, and travel speed of the 308L groove weld were 240 A, 10.4 V, and 9.4 cm/min, respectively. A PWHT was not performed for the 308L groove weld, consistent with industry practice.

B. *Neutron Diffraction Residual Stress Measurement*

Neutron diffraction was used to characterize the residual stresses of the DMW using the VULCAN engineering materials diffractometer at the Spallation Neutron Source (SNS) at Oak Ridge National Laboratory.[23] The SNS is a pulsed neutron source and all neutron detection events are recorded as discrete events in both time (energy) and scattering angle. The time-of-flight VULCAN diffractometer enables measuring lattice strain in multiphase materials simultaneously. The configuration of the experiment is shown in

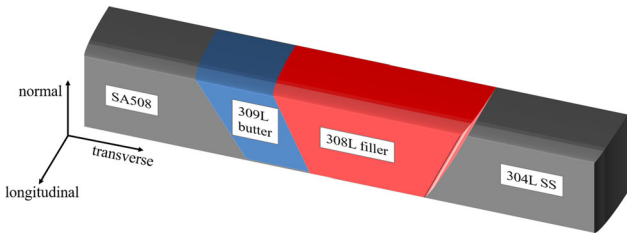

Fig. 1—Schematic illustration of the SA508-SS 304L DMW with SS 308L filler and SS 309L butter. The longitudinal direction corresponds to the weld bead direction. The weld bevel angle is 60 degrees.

Table 1. Composition (Weight Percent) of the Materials in the DMW, with Fe as Balance

Materials	Cr	Ni	Mn	Mo	Si	Cu	N	C	Cr_{eq}	Ni_{eq}
SA508	0.2	0.8	1.4	0.52	0.23	0.09	n/a	0.22	0.7	8.5
309L	23.0	13.7	1.6	0.07	0.47	0.10	~ 0.05‡	0.01	23.1	15.1
308L	19.9	10.4	2.0	0.15	0.52	0.28	~ 0.05‡	0.016	20.0	12.0
304L	18.1	8.1	1.7	0.33	0.28	0.44	0.07	0.02	18.4	10.2

‡A nitrogen concentration of 0.05 pct is assumed for SS 308L and 309L for the equivalent Cr and Ni composition calculation.

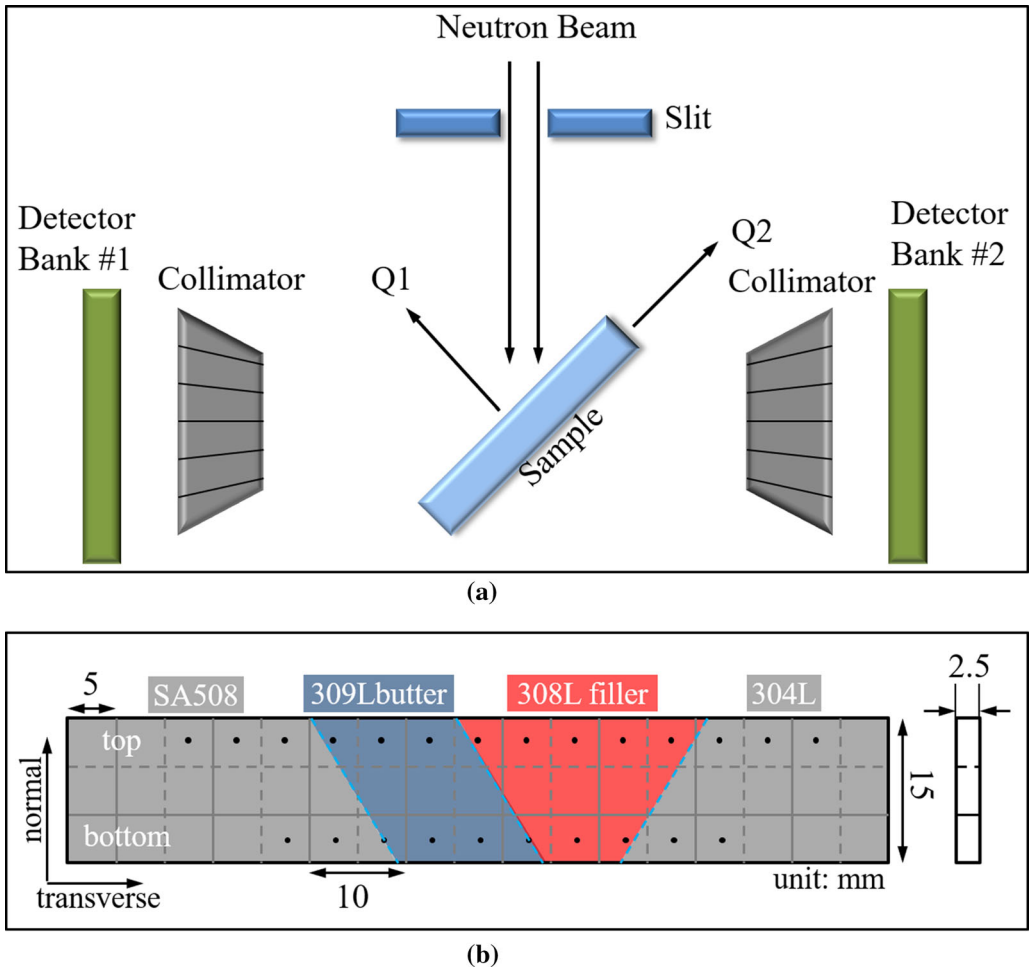

Fig. 2—(*a*) Configuration of the VULCAN engineering materials diffractometer, with two detector banks defining two wavevector transfers, Q1 and Q2, along the sample (Q2) and in the orthogonal direction (Q1), and (*b*) Schematic of the reference sample for neutron diffraction measurements at the cuboids indicated by the dots. The samples for residual stress measurements were a section from the middle of the entire weldment piece.

Figure 2(a). Two detector banks define two wavevector transfer directions, Q1 and Q2 which allow lattice strains to be simultaneously measured in two directions. A 90 deg rotation of the sample about the transverse direction was required to measure the lattice spacing in the third direction for the residual stress calculation. A nominal $2 \times 3 \times 2$ mm^3 neutron gauge volume was used for the all the measurements. The lattice spacing of specific (*hkl*) lattice planes was determined by fitting the diffraction neutron spectra using VULCAN Data Reduction and Interactive Visualization (VDRIVE) software.

Residual stress measurement requires a stress-relieved reference sample with identical composition. In analogy to the published work of residual stress measurement using the same diffractometer,[24] a comb sample was fabricated in which $5 \times 5 \times 2.5$ mm^3 cuboids were attached along a thin edge, which in principle relieved residual stress from the welding process.[24] A schematic illustration of the reference sample is shown in Figure 2(b) with the solid lines and dashed lines representing the cuts on two faces of the sample. Neutron diffraction measurements were targeted at the center of each comb sample cuboid, indicated by dots in

Figure 2(b), with the identical probing arrangement on the DMW sample. The measurements were performed on the top and the bottom cuboids, including the measurements close to the fusion boundary of SA508-309L, which represented the largest composition and lattice mismatch. δ-ferrite precipitates with < 10 pct volume fraction were observed with microscopy techniques in 309L, 308L, and 304L (as will be shown in Section III–A), and the residual stress within the δ-ferrite was not calculated due to negligible diffraction intensity. Therefore, only residual stress of the austenitic matrix was calculated in 309L, 308L, and 304L.

The residual stress was calculated using Eq. [1], where E and v are Young's Modulus and Poisson's ratio, respectively, ε_i is the lattice strain in the i direction (transverse, longitudinal, and normal), which was calculated based on Eq. [2], and $d_{o,i}$ and d_i are the lattice spacing of the reference and DMW samples, respectively. In this work, (211) reflection for ferritic matrix (SA508) and the (311) reflection for austenitic matrix (308L, 309L, and 304L) were selected for the strain calculation because these reflections have the smallest interference from the intragranular strain.[25] The values for Young's Modulus and Poisson's ratio were 216 GPa and 0.27, respectively, for SA508[26] and 184 GPa and 0.29 for austenitic phases.[27] The errors for the strain and stress were determined by the error propagation from the fitting errors.

$$\sigma_i = \frac{E}{(1+v)}\left\{\varepsilon_i + \frac{v}{1-2v}\sum_{j=1}^{3}\varepsilon_j\right\} \quad [1]$$

$$\varepsilon_i = \frac{d_i}{d_{o,i}} - 1 \quad [2]$$

C. *Microstructures Characterization*

Grain morphology and precipitates were characterized primarily using electron backscatter diffraction (EBSD) and scanning electron microscopy (SEM). Samples for EBSD were prepared using the standard metallography procedures with the final step of vibration polishing using a 0.05 um Al_2O_3 solution. Precipitate observation was performed by etching the SA508 material with 2 pct Nital solution after the polishing procedure. A Thermo Scios2 Dual-Beam SEM/FIB with a Hikari Super EBSD detector was used for EBSD data acquisition. The EBSD analysis was performed using the Analysis OIM (orientation imaging microscopy) software for phase distribution, inverse pole figure (IPF), grain boundary character, and kernel average misorientation (KAM). Grain boundaries were categorized into low-angle grain boundary (LAGB, 5–15 deg), high-angle grain boundary (HAGB, > 15 deg), and coincidence site lattice (CSL) boundary. CSL boundary categorization followed the Palumbo–Aust criterion,[28] with the maximum allowable deviation angle $\Delta\theta = 15^{\circ}/\Sigma^{5/6}$, where Σ is the CSL number. KAM represents the misorientation of the measured Kikuchi patterns from the theoretical unstrained patterns of the indexed phase, which is an indication of defects population, primarily the dislocation density.[29] In this work, KAM was calculated for the first nearest neighbor with the maximum misorientation of 5 deg.

D. *Vickers Hardness Measurement*

Vickers hardness measurements were performed across the weldment, with the applied force of 1 kilogram-force and the dwelling time of 15 second. Spacings between the indents were 0.9 to 1.5 mm with smaller spacing near the fusion boundary due to the expected larger gradient. Average hardness of three indents are reported in this work.

III. RESULTS

A. *Microstructure*

The grain morphology of the fusion boundary near 304L-308L is shown in Figure 3. Both 304L and 308L demonstrate an austenitic matrix with δ-ferrite precipitates. The δ-ferrite precipitates in the 304L HAZ are in the form of stringers. The formation of δ-ferrite precipitates is not the product of thermal cycling associated with the welding processing, but instead the hot rolling process. These precipitates were also observed in 304L base materials. In the 308L fusion zone, large austenitic grains are elongated along the heat dissipated direction. Intragranular δ-ferrite precipitates in 308L fusion zone have a skeletal morphology, as shown in the enlarged phase distribution and IPF maps in the inset of Figure 3. δ-ferritic precipitates have higher Cr (~ 30 wt pct) but lower Ni (~ 6 wt pct) compositions, compared to the austenite matrix (~ 20 wt pct Cr and ~ 10 wt pct Ni), as Cr promotes while Ni inhibits the ferrite formation. A volume fraction of ~ 9 pct ferrite phase is predicted in 308L fusion zone based on the WRC-1992 constitution diagram,[22,30] and this is consistent with our EBSD measurement, where the area fraction of δ-ferrite in the fusion zone was measured as 8.8 pct.

The 309L butter exhibits two distinct microstructure morphologies; a non-uniform dilution zone with the width of ~ 1 to 4 mm adjacent to the fusion boundary of SA508-309L and a duplex zone away from the fusion boundary, as shown in Figure 4(a), with the inset exhibiting the morphology of the duplex zone in 309L. The duplex zone of 309L has similar skeletal δ-ferrite morphology as 308L, whereas the dilution zone is characterized by a single austenitic phase. Composition profiles across different zones in Figure 4(c) show the reduced Cr and Ni compositions in the dilution zone compared to those in the duplex zone. However, the absence of the ferrite phase in the dilute zone cannot simply attributed to the 3 pct Cr (as a ferrite-promoting element) reduction according to the WRC-1992 diagram.[22] We believed that carbon (as an austenite-promoting element) diffusion from the SA508 into the 309L butter could also contribute to the absence of δ-ferrite

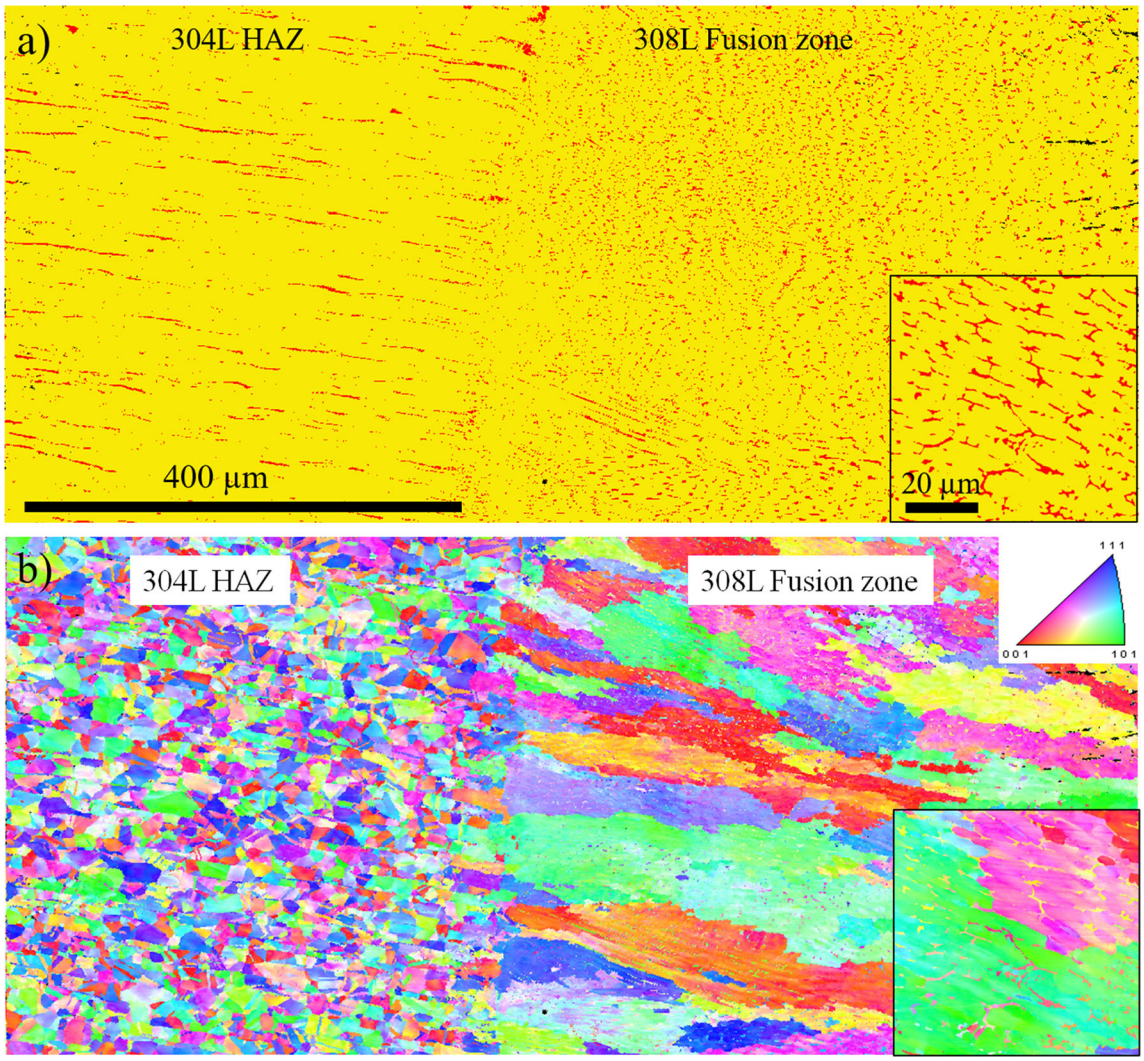

Fig. 3—(*a*) Phase distribution of austenitic matrix (yellow) and δ-ferritic precipitates (red), and (*b*) Inverse pole figure across the 304L–308L fusion boundary, with the inset of the larger magnification images on the 308L fusion zone. The orientation triangle holds for the IPFs throughout the manuscript (Color figure online).

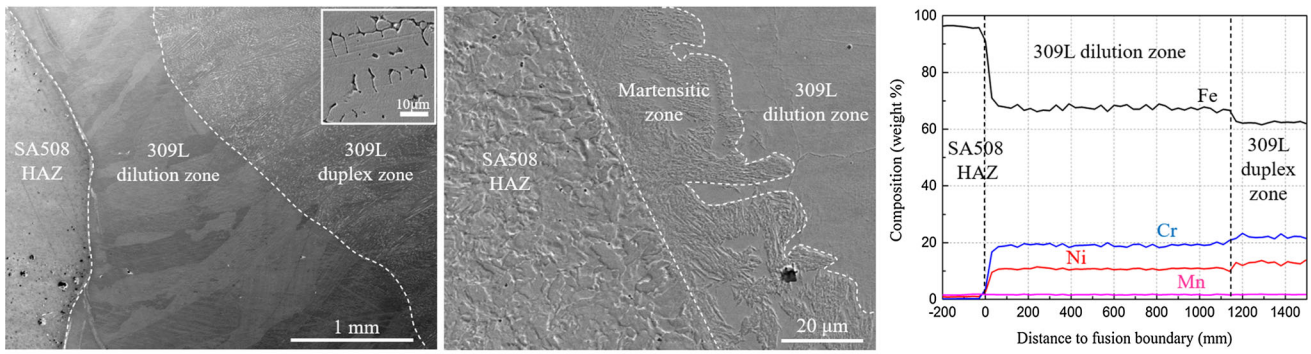

Fig. 4—Microstructure of the fusion boundary of SA508–309L. (*a*) 309L demonstrates two morphologies (dilution zone and duplex zone) with the composition profiles shown in (*c*) and the inset showing an enlarged image of the 309L duplex zone; (*b*) martensitic zone at the fusion boundary.

precipitates at the dilution zone. However, the carbon composition was not measured due to its low composition and its low sensitivity in the EDS measurement.

A ~ 20 to 30-μm-wide martensitic zone with irregular boundaries is present at the fusion boundary, as shown in Figure 4(b). The complex structure of the martensitic zone inspires more detailed microstructure analysis. Figures 5(a) and (b) show the phase distribution and the IPF maps near the fusion boundary. The grain morphology in proximity of the fusion boundary is complex and consists of refined grains. Although the interface of the martensitic zone and the SA508 HAZ is not distinct from the IPF map, smaller grains of irregular shape are present within ~ 25 μm of the fusion boundary, which likely corresponds to the martensitic zone. Figures 5(c) and (d) show the scanning transmission electron microscope dark-field image and the combined Cr/Ni maps near the fusion boundary. Cr-rich carbide precipitates and Ni-rich regions are observed at the martensitic zone. The Cr-rich carbide precipitates have an average size and a number density of 44 ± 17 nm and 1.5×10^{21} m^{-3}, corresponding to a local volume fraction of ~ 10 pct. In contrast, only a few ~ 10 nm Cr-rich precipitates were observed in 309L.

B. *Vickers Hardness Measurement*

Figure 6 shows the Vickers hardness profile across the weldment. Vickers hardness measurements were also

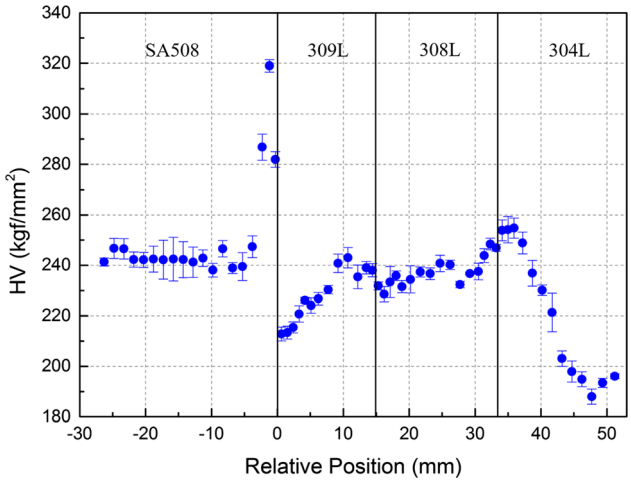

Fig. 6—Vickers hardness across the weldment, showing that the widths of HAZ are 4 mm and 16 mm for SA508 and 304L, respectively.

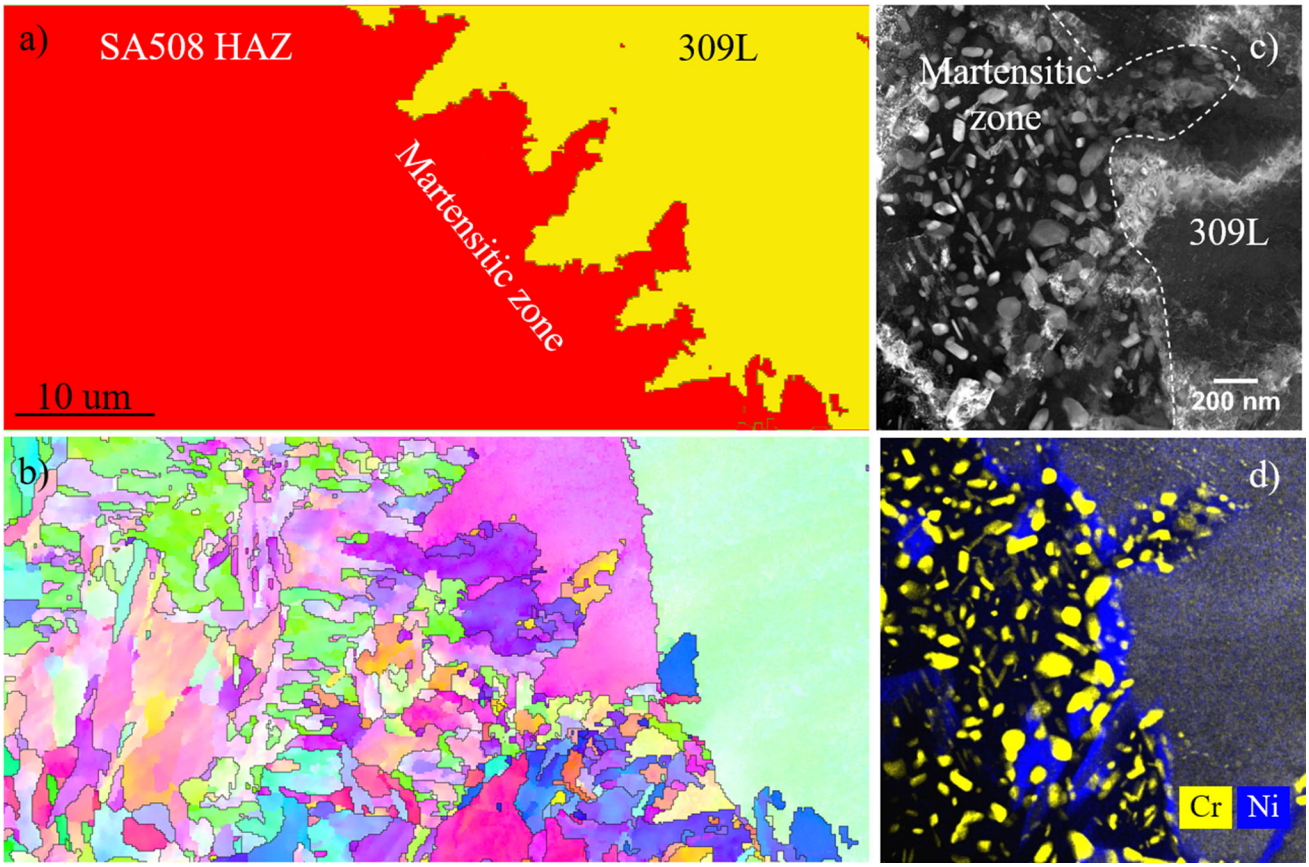

Fig. 5—(*a*) Phase distribution of 309L (yellow) and SA508 HAZ (red), and (*b*) Inverse pole figure of the region near fusion boundary. (*c*) STEM dark-field image and (*d*) combined maps of Cr (yellow) and Ni (blue) at the fusion boundary of SA508-309L (Color figure online).

performed at the SA508 and 304L base materials, with the hardness of 245.1 ± 5.4 HV_1 and 190.9 ± 3.6 HV_1 for the SA508 and 304L, respectively. Thermal cycling associated with the welding process increased the hardness of the HAZ of both ends, and the width of HAZ was 4 mm and 16 mm for SA 508 and 304L, respectively. In the SA508 HAZ, a maximum hardness (319.0 ± 2.5 HV_1) was observed at about 1.2 mm from the fusion boundary, and the hardness decreased toward the fusion boundary. As mentioned earlier, carbon diffusion from SA508 to 309L lead to carbon enrichment at 309L and thus the formation of a dilution zone. Such diffusion also lead to carbon depletion at SA508 HAZ near fusion boundary, which could contribute to reduced the hardness near the fusion boundary. The mechanisms leading to the increased hardness in HAZ will be discussed in Section IV.

C. *Residual Stress Measurements*

The residual stress measurements across the weldment at top and bottom layers are shown in Figure 7. Residual stress in the base SA508 and 304L is uniformly small in three directions (mostly ≤ 50MPa in compression), while the residual stresses are complex within the weldment. The 308L fusion zone shows variations of residual stress ranging from 300 MPa tensile stress to 200 MPa compressive stress. The 309L/308L fusion boundary also demonstrates complex stress distribution, with up to 200 MPa tensile stress at the top layer, while compressive stress at the bottom layer. Such complex residual stress distributions are consistent with the EBSD results of a similar weldment that exhibits heterogeneous and complex KAM distribution (an indication of strain distribution) within the fusion zone .[7] Large residual stress is present in 309L, especially near the fusion boundary (up to ~ 750 MPa in tension), while SA508 shows up to ~ 200 MPa in compression in longitudinal and normal directions near the fusion boundary. Larger cracking growth rate was usually observed in regions of large tensile residual stress.[31,32] The large tensile residual stress at the 309L indicates its high cracking susceptibility, consistent with the observation of the crack initiation in 309L weld metal in a recently published work on a similar weldment.[3]

A comb reference sample was used to obtain the stress-relieved reference lattice spacing. Ideally, lattice spacing in three direction should be equivalent within the instrument resolution (~ 1.5×10^{-4} Å for our VULCAN diffractometer measurement parameters) for a completely stress-relieved reference sample. However, it is very challenging to completely relieve residual stress in metals with a complex microstructure of multiple phases. Figure 8 shows the lattice spacing d_o of (211) reflection of ferritic phase (on the left axis) and of (311) reflection of austenitic phase (on the right axis) of the

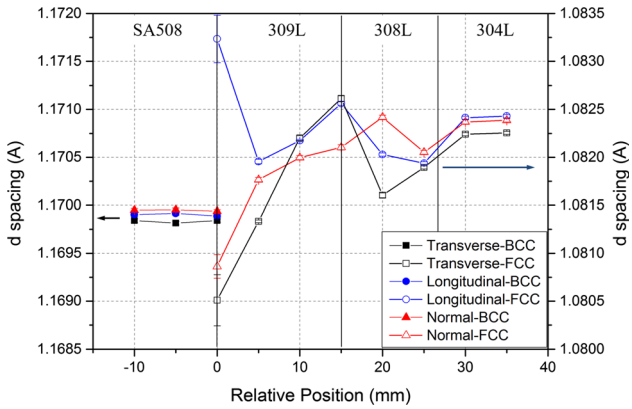

Fig. 8—Lattice spacing d_o at the bottom layer of the reference comb sample. The large variation in lattice spacing within the 309L weldment butter indicates residual stress persists in the comb reference within the 309L, especially near the SA508–309L interface.

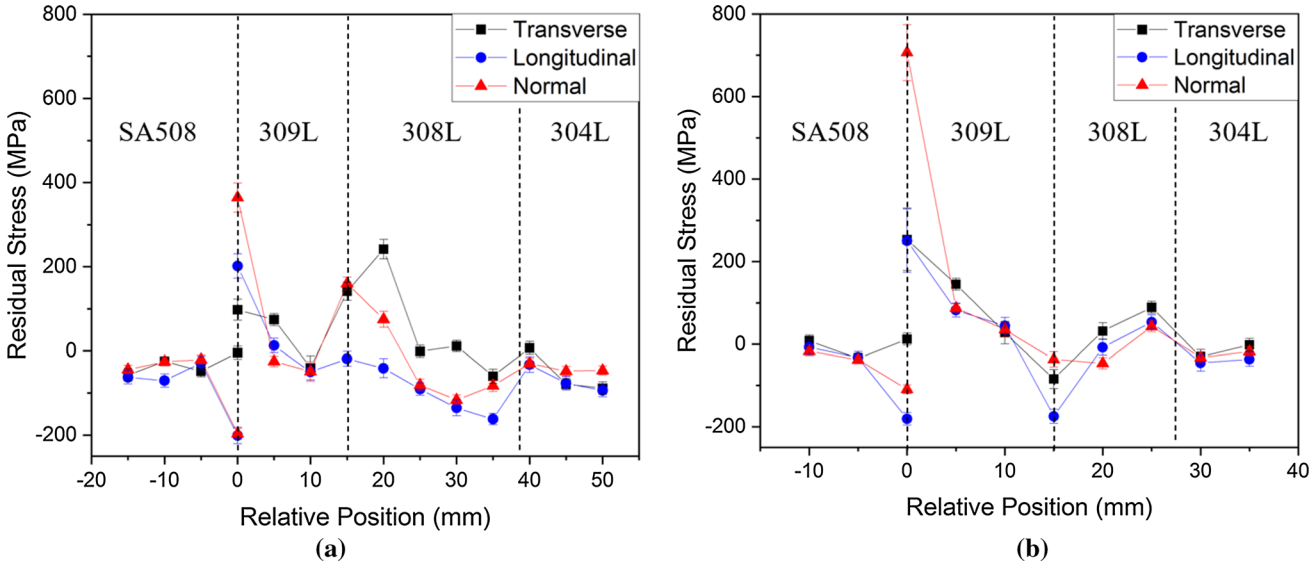

Fig. 7—Residual stress across the weldment at the (*a*) top layer, and (*b*) bottom layer. Large tensile stress (up to 750 MPa) is present at 309L while mild compressive stress (up to 200 MPa) is present at SA508 near the fusion boundary of SA508–309L.

reference sample. The base materials show consistent d spacing in all three directions. However, the fusion zone shows some variation of lattice spacing, especially near the fusion boundary of SA508-309L, indicating the persistent residual stress in the comb reference.

The persistent residual stress in the reference sample may imply that the locally high residual stress is difficult to fully relieve. This locally high residual stress is likely originated from a mixture of phases (austenitic matrix and δ ferrite in 308L/309L) and from the interface of two components with mismatch of lattice, composition, and thermal expansion (fusion boundary of SA509/309L). The lack of complete relief of the residual stress makes quantification of residual stress difficult in this region of the weldment. However, we observed the general trends of largest tensile stress in the 309L portion of the weldment and mild compressive stress at SA508 near the fusion boundary. Residual stresses in weldments are a complex effect from non-uniform thermal expansion of temperature change and the phase transformation. Constrained thermal contraction from cooling leads to tensile stress in the HAZ and the fusion zone. Austenitic steels generally demonstrate much higher thermal expansion (by ~ 30 to ~ 60 pct) than the low-alloy steels,[33] leading to larger tensile stress in the fusion zone. In addition, volume expansion of solid-state phase transformation from the close-packed austenite (FCC phase) to α-ferrite (BCC phase) in SA508 counteracts against the thermal contraction and leads to an accumulation of compressive stress in the SA508 HAZ.

IV. DISCUSSION

Changes of the hardness were observed in the HAZ of both 304L and SA508. To provide a mechanistic understanding of this hardness change, microstructures were characterized in the HAZ and base metals, and correlated with the increased hardness.

Figure 9 shows the grain morphology of 304L base metal (a-c) and the HAZ (d-f). HAZ exhibits equiaxed grain morphology with δ-ferrite at grain boundary, similar to the base metal. Average grain sizes are comparable, being 24.0 ± 3.2 μm and 25.0 ± 4.6 μm for the base and HAZ, respectively. Grain boundary character maps in Figures 9(c) and (f) show the distribution of high angle (HAGB, in black), low angle (LAGB, in blue), and coincidence site lattice (CSL, in red) boundaries with their respective fractions of 65.1 (64.0), 4.5 (0.6), and 30.4 (35.4) for the base (HAZ). HAZ demonstrates higher CSL (primarily $\Sigma 3$) with lower LAGB fraction. Grain boundary character distribution, especially CSL affected the yield strength and

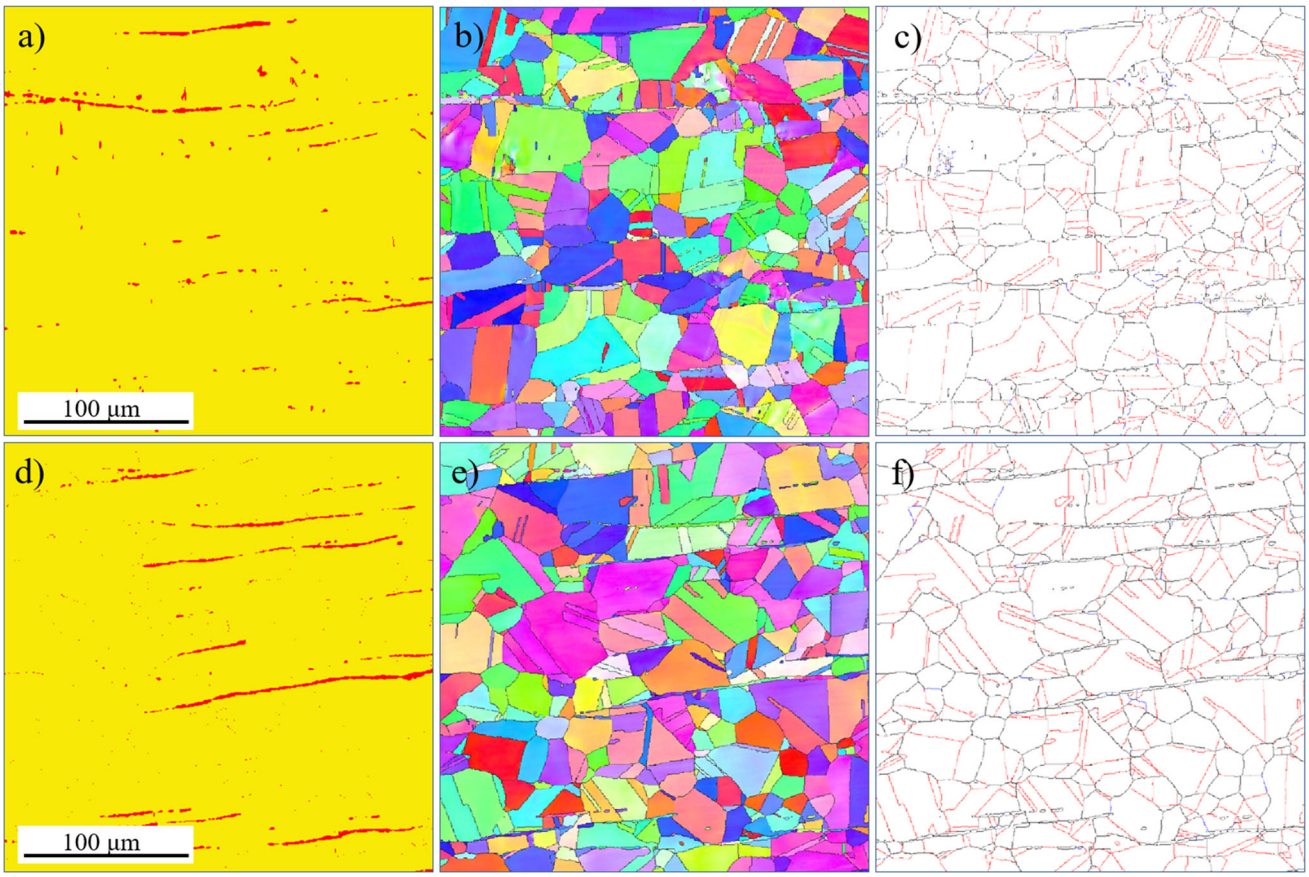

Fig. 9—(*a*) and (*d*) Phase distribution of austenite matrix (yellow) and δ-ferrite precipitates (red); (*b*) and (*e*) Inverse pole figures; (*c*) and (*f*) grain boundary character distribution for the 304L base (top row, a–c) and 304L HAZ (bottom row, d–f). Grain boundaries in c) and f) are HAGB (black), LAGB (blue), and CSL (red) (Color figure online).

hardness,[34] and austenitic steels with a higher CSL fraction tend to be harder.[35] Although quantification of hardening from increased CSL fraction was difficult and has not been reported for SS 304L to our best knowledge, 5 pct increment of CSL fraction is expected to have small contribution.[36] In addition, EBSD analysis indicates a higher average KAM in the HAZ (0.38) than in the base (0.31), which is an indication of higher dislocation density in the HAZ. Higher dislocation density was directly observed in the SS 316 HAZ in a similar DMW SA508-SS 316 with Ni-based filler/butter using electron microscopy.[37] No precipitates were observed other than δ-ferrite precipitates, and 304L HAZ exhibited a similar distribution of δ-ferrite precipitates as the base. Therefore, the EBSD analysis indicates that the increased hardness in the 304L HAZ is mainly attributed to the higher dislocation density with some minor contribution from higher CSL fraction.

A change of grain morphologies was observed at different regions of SA508 HAZ, as shown in Figure 10. These regions correspond to coarse-grain HAZ (CGHAZ), fine-grain HAZ (FGHAZ), inter-critical HAZ (ICHAZ), and base material, respectively, in the ascending order of distance from the fusion boundary. The various grain morphologies are primarily attributed to the different peak temperatures and the cooling rates.[38,39] A phase transformation to austenite occurred when the peak temperature rose above the austenite transformation temperature A_{C1}. Larger prior austenite grains (CGHAZ compared to FGHAZ) were attributed to the higher peak temperature at CGHAZ. The ICHAZ had a peak temperature between A_{C1} and A_{C3}, with a partial phase transformation to austenite leading to mixed grain morphologies of newly formed prior austenite grains and coarse grains similar to the SA508 base. Average grain sizes for different regions are

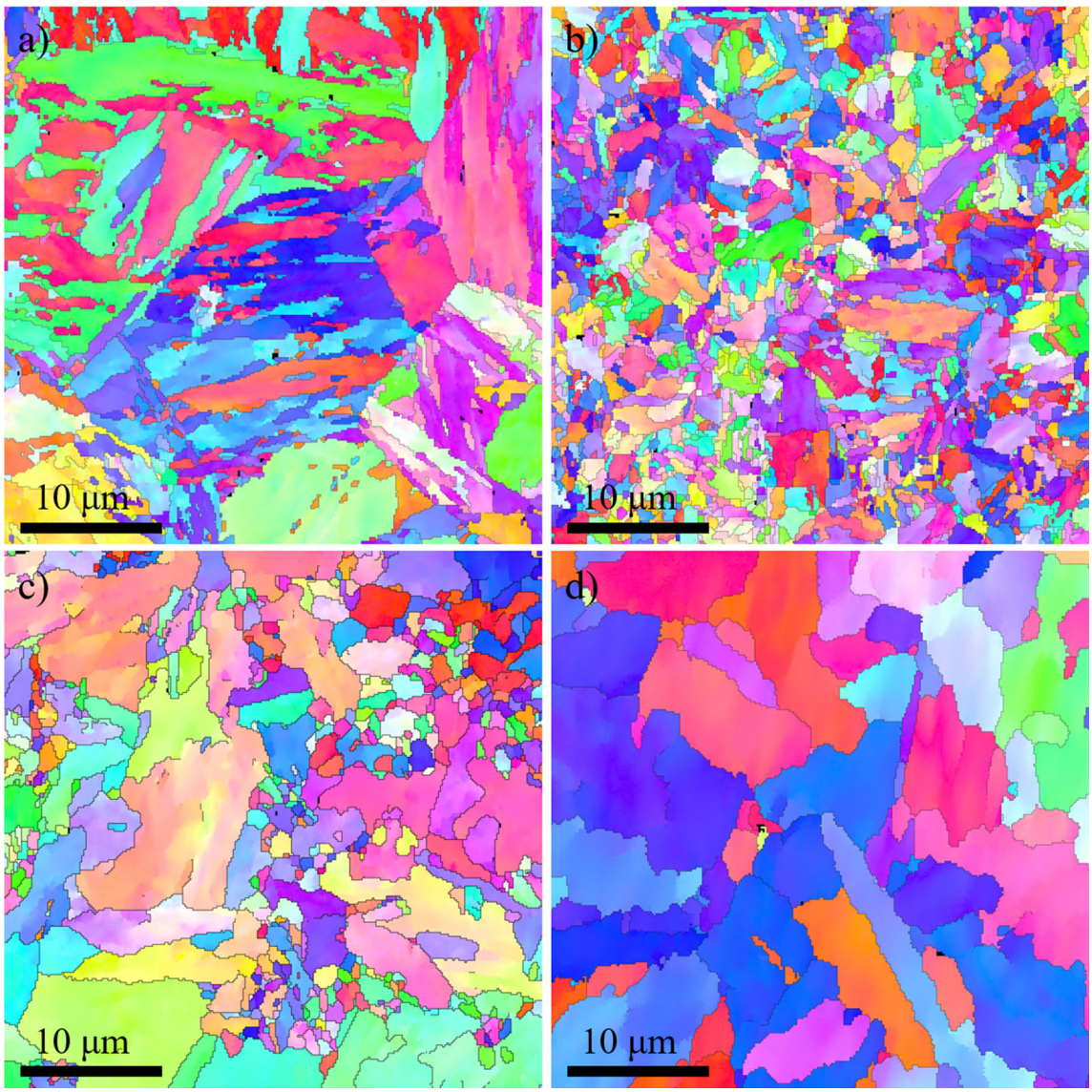

Fig. 10—Inverse pole figures of the different regions at (*a*) coarse-grain HAZ, (*b*) fine-grain HAZ, (*c*) inter-critical HAZ, (*d*) base material SA508 with the same magnification.

Table II. Average Grain Size, Average KAM at CGHAZ, FGHAZ, IGHAZ, and Base of SA508

Region	CGHAZ	FGHAZ	ICHAZ	Base
Average Grain Size (μm)	1.6 ± 0.7[†]	1.1 ± 0.4	1.0 ± 0.5 (~ 25 pct[††]) 4.5 ± 2.5 (~ 75 pct[††])	4.3 ± 1.8
Average KAM (°)	0.78	0.79	0.53	0.34

[†]The average width of the lath structure of CGHAZ.
[††]Area fraction of different grains inside ICHAZ.

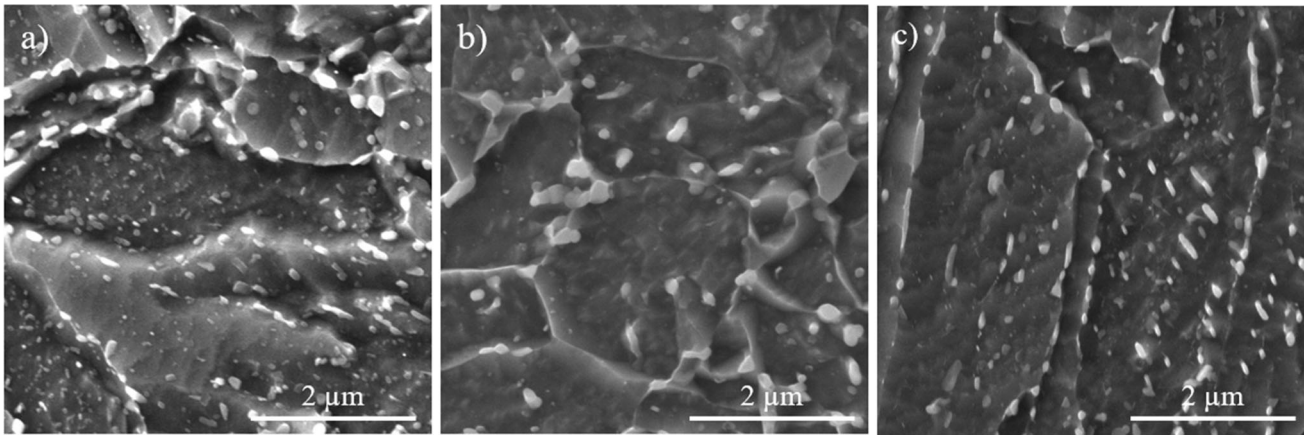

Fig. 11—Precipitates (shown as white features) in (*a*) CGHAZ, (*b*) FGHAZ, (*c*) SA508 base, showing largest precipitate density in the CGHAZ.

summarized in Table II. Both CGHAZ and FGHAZ exhibited smaller grain size than the SA508 base material, and the ICHAZ showed a mixture of grains, with ~ 25 pct area of FCHAZ-like grain morphology, and ~ 75 pct area of base-like grain morphology. Average KAM was also analyzed for different regions and are included in Table II. The HAZ had larger KAM values compared to the base material and was greatest in the FGHAZ and CGHAZ. This indicated a larger dislocation density in HAZ due to the thermal cycling.

Precipitates with different number densities were observed in different regions of HAZ. Figure 11 shows the precipitates distributions (likely carbides, as reported in the SA508 base and HAZ[40,41]) in CGHAZ, FGHAZ, and base. The largest number density of precipitates was observed in CGHAZ, with coarse precipitates at boundaries and fine precipitates inside grains. The FGHAZ exhibited a distribution of precipitates primarily at boundaries with a reduced density. Precipitation is the consequence of the thermal history and the volume fraction of carbide precipitates in a simulated HAZ of SA508 was studied at various peak temperatures.[42] Unfortunately, no systematic trend was observed for the volume fraction of carbide precipitates, which also depended on PWHT.[42] However, the observation of the higher number density of precipitates in CGHAZ in this work indicates stronger precipitate strengthening effect than in FGHAZ.

The increased hardness in the SA508 HAZ is a complex phenomenon that is attributed to multiple mechanisms. Grain morphology with reduced grain size, higher dislocation density, and higher precipitate density were observed in the SA508 HAZ, leading to enhancing grain boundary, dislocation, and precipitate strengthening effects, which resulted in greater hardness in the SA508 HAZ. However, quantification of all strengthening effect cannot be achieved using SEM and EBSD. For example, although KAM is indication of dislocation density, the current method of dislocation density estimation from KAM is related to EBSD measurement parameters (such as step size),[43] while the dislocation density is an intrinsic property. Such quantification based on KAM leads to uncertainty in dislocation density quantification. In addition, quantification of precipitate strengthening effect is based on the volume number density, which is difficult to measure based on a two-dimensional SEM image. Quantification of strengthening contribution might be achievable with the aid of TEM, where dislocation density, size distribution, and number density of precipitates can be directly measured for strengthening contribution estimation.

V. CONCLUSION

Microstructure, hardness, and residual stress distribution are investigated for a SA508–309L/308L–304L DMW using primarily SEM/EBSD, Vickers indentation, and neutron diffraction techniques. Increased hardness is observed in HAZ, and this change of hardness is correlated with the microstructure evolution. The major findings are summarized as follows:

1. Higher hardness is measured in the HAZ of both SA508 and 304L with different contributing

mechanisms. Detailed EBSD analysis demonstrates that SA508 HAZ exhibits different grain morphologies, while 304L HAZ maintains similar grain morphology as the base material. The higher hardness at SA508 HAZ is attributed to the refined grain morphology, higher dislocation density, and higher number density of precipitates, while the higher hardness at 304L HAZ is primarily attributed to the higher dislocation density.

2. Narrow martensitic zone with the width of ~ 20 to 30 μm is observed at the fusion boundary of SA508-309L, where Cr-rich carbide precipitates are observed with the average size and number density of 44.1 ± 16.9 nm and 1.5×10^{21} m^{-3}, respectively.
3. 309L butter demonstrates two different grain morphologies, with the duplex zone that has similar morphology as 308L filler and the dilution zone that consists of single austenitic phase. The absence of δ-ferrite at the dilution zone is likely attributed to the higher carbon content diffused from SA508.
4. Residual stress is measured by the neutron diffraction. Although residual stress is not completely relieved at the fusion zone in the reference sample likely due to the interphase constrains, the general trend of the residual stress can be learned from this work. Both base materials demonstrate negligible compression stress (< 50 MPa), while 308L fusion zone exhibits complex stress distribution with tensile stress and compressive stress at different regions. Largest tensile residual stresses and stress gradients are observed within the 309L butter, especially near the fusion boundary. Such high tensile residual stress implies the highest cracking susceptibility of 309L, consistent with the previous observation of the crack initiation in 309L metal weld in similar weldments.

ACKNOWLEDGMENTS

This work was supported by the US Department of Energy Nuclear Energy University Programs under contract number DE NE0008699. The research was carried out in part in the Materials Research Laboratory Central Research Facilities, University of Illinois. The research used resources at the Spallation Neutron Source, a DOE Office of Science User Facility operated by the Oak Ridge National Laboratory. In addition, W. Z. is grateful to Yiyu Wang (ORNL) for sample preparation and active discussion.

REFERENCES

1. J.C. Lippold and D.J. Kotecki: *Welding Metallurgy and Weldability of Stainless Steels*, Wiley, New York, 2005.
2. G. Mirshekari, E. Tavakoli, M. Atapour, and B. Sadeghian: *Mater. Des.*, 2014, vol. 55, pp. 905–11.
3. L. Dong, C. Ma, Q. Peng, E.-H. Han, and W. Ke: *J. Mater. Sci. Technol.*, 2020, vol. 40, pp. 1–14.
4. G. Li and J. Congleton: *Corros. Sci.*, 2000, vol. 42, pp. 1005–21.
5. J. Hou, Q. Peng, Y. Takeda, J. Kuniya, and T. Shoji: *Corros. Sci.*, 2010, vol. 52, pp. 3949–54.
6. Z. Chen, Y. Lu, X. Ding, and T. Shoji: *Mater. Charact.*, 2016, vol. 121, pp. 166–74.
7. H. Ming, Z. Zhang, J. Wang, E.-H. Han, and W. Ke: *Mater. Charact.*, 2014, vol. 97, pp. 101–15.
8. T. Sarikka, M. Ahonen, R. Mouginot, P. Nevasmaa, P. Karjalainen-Roikonen, U. Ehrnsten, and H. Hanninen: *Int. J. Press. Vessels Pip.*, 2017, vol. 157, pp. 30–42.
9. W. Wang, Y. Lu, X. Ding, and T. Shoji: *Mater. Charact.*, 2015, vol. 107, pp. 255–61.
10. J. Francis, W. Mazur, and H. Bhadeshia: *Mater. Sci. Technol.*, 2006, vol. 22, pp. 1387–95.
11. W.-C. Chung, J.-Y. Huang, L.-W. Tsay, and C. Chen: *Mater. Trans.*, 2011, vol. 52, pp. 12–19.
12. J. Hou, Q. Peng, Y. Takeda, J. Kuniya, T. Shoji, J. Wang, E.-H. Han, and W. Ke: *J. Mater. Sci.*, 2010, vol. 45, pp. 5332–38.
13. K. Mao, H. Wang, Y. Wu, V. Tomar, and J.P. Wharry: *Mater. Sci. Eng., A*, 2018, vol. 721, pp. 234–43.
14. Y. Feng, Z. Luo, Z. Liu, Y. Li, Y. Luo, and Y. Huang: *Mater. Des.*, 2015, vol. 85, pp. 24–31.
15. S. Sabooni, F. Karimzadeh, M. Enayati, A. Ngan, and H. Jabbari: *Mater. Charact.*, 2015, vol. 109, pp. 138–51.
16. S. Kumar and A. Shahi: *Mater. Des.*, 2011, vol. 32, pp. 3617–23.
17. P. Sedek, J. Brozda, L. Wang, and P. Withers: *Int. J. Press. Vessels Pip.*, 2003, vol. 80, pp. 705–13.
18. V. Satyanarayana, G.M. Reddy, and T. Mohandas: *J. Mater. Process. Technol.*, 2005, vol. 160, pp. 128–37.
19. A. Joseph, S.K. Rai, T. Jayakumar, and N. Murugan: *Int. J. Press. Vessels Pip.*, 2005, vol. 82, pp. 700–05.
20. C. Shiga, H.Y. Yasuda, K. Hiraoka, and H. Suzuki: *Weld. World*, 2010, vol. 54, pp. R71–79.
21. W. Woo, V. Em, C.R. Hubbard, H.-J. Lee, and K.S. Park: *Mater. Sci. Eng., A*, 2011, vol. 528, pp. 8021–27.
22. D. Kotecki and T. Siewert: *Weld. J.*, 1992, vol. 71, pp. 171–78.
23. K. An, H.D. Skorpenske, A.D. Stoica, D. Ma, X.-L. Wang, and E. Cakmak: *Metall. Mater. Trans. A*, 2011, vol. 42, pp. 95–99.
24. J.-A.J. Wang, E.A. Payzant, J.R. Bunn, and K. An: *Neutron Residual Stress Mapping for Spent Nuclear Fuel Storage Canister Weldment*, Oak Ridge National Lab.(ORNL) No. ORNL/TM-2018/827, Oak Ridge, TN, 2018..
25. M.T. Hutchings, P.J. Withers, T.M. Holden, and T. Lorentzen: *Introduction to the Characterization of Residual Stress by Neutron Diffraction,* CRC Press, 2005.
26. A. Mark, J. Francis, H. Dai, M. Turski, P. Hurrell, S. Bate, J. Kornmeier, and P. Withers: *Acta Mater.*, 2012, vol. 60, pp. 3268–79.
27. R. Moat, H. Stone, A. Shirzadi, J. Francis, S. Kundu, A. Mark, H. Bhadeshia, L. Karlsson, and P. Withers: *Sci. Technol. Weld. Joining*, 2011, vol. 16, pp. 279–84.
28. G. Palumbo, K. Aust, E. Lehockey, U. Erb, and P. Lin: *Scri. Mater.*, 1998, vol. 38, pp. 1685–90.
29. K. Fujiyama, K. Mori, D. Kaneko, H. Kimachi, T. Saito, R. Ishii, and T. Hino: *Int. J. Press. Vessels Pip.*, 2009, vol. 86, pp. 570–77.
30. A. Putz, M. Althuber, A. Zelic, E. Westin, T. Willidal, and N. Enzinger: *Weld. World*, 2019, vol. 63, pp. 1075–86.
31. F.W. Brust and P.M. Scott: *ASME Pressure Vessels and Piping Conference*, 2007.
32. C. Jang, P.-Y. Cho, M. Kim, S.-J. Oh, and J.-S. Yang: *Mater. Des.*, 2010, vol. 31, pp. 1862–70.
33. Q. Wang, M. Zhang, W. Liu, X. Wei, J. Xu, J. Chen, H. Lu, and C. Yu: *J. Mater. Process. Technol.*, 2017, vol. 247, pp. 64–72.
34. L. Tan, L. Rakotojaona, T.R. Allen, R.K. Nanstad, and J.T. Busby: *Mater. Sci. Eng. A*, 2011, vol. 528 (6), pp. 2755–61.
35. L. Tan, K. Sridharan, T.R. Allen, R.K. Nanstad, and D.A. McClintock: *J. Nucl. Mater.*, 2008, vol. 374 (1–2), pp. 270–80.
36. T. Liu, Q. Bai, X. Ru, S. Xia, X. Zhong, Y. Lu, and T. Shoji: *Mater. Sci. Technol.*, 2019, vol. 35, pp. 477–87.
37. J.W. Kim, K. Lee, J.S. Kim, and T.S. Byun: *J. Nucl. Mater.*, 2009, vol. 384, pp. 212–21.

38. Y. Wang, R. Kannan, and L. Li: *Mater. Charact.*, 2016, vol. 118, pp. 225–34.
39. W. Guo, S. Dong, J.A. Francis, and L. Li: *Mater. Sci. Eng.A*, 2015, vol. 625, pp. 65–80.
40. B. Lee, M. Kim, J. Yoon, and J. Hong: *Int. J. Press. Vessels Pip.*, 2010, vol. 87, pp. 74–80.
41. S. Lee, S. Kim, B. Hwang, B. Lee, and C. Lee: *Acta Mater.*, 2002, vol. 50, pp. 4755–62.
42. S. Kim, S.Y. Kang, S. Lee, S.J. Oh, S.-J. Kwon, O.H. Kim, and J.H. Hong: *Metall Mater Trans A*, 2000, vol. 31, pp. 1107–19.
43. M. Calcagnotto, D. Ponge, E. Demir, and D. Raabe: *Mater. Sci. Eng. A*, 2010, vol. 527, pp. 2738–46.